

https://dspace.org/

Planar Deposition via In Situ Conversion Engineering for DendriteFree Zinc Batteries

Hanning Zhang; Y You; Dawei Sha; T Shui; Nosipho Moloto ...

WILEY-V C H VERLAG GMBH
https://hdl.handle.net/10539/43706
WOS

Downloaded from a DSpace repository. https://dspace.org/

Check for updates

ADVANCED MATERIALS
www.advmat.de

Planar Deposition via In Situ Conversion Engineering for Dendrite-Free Zinc Batteries

Hanning Zhang, Yurong You, Dawei Sha, Tao Shui, Nosipho Moloto, Jiacheng Liu, Song-Zhu Kure-Chu, Takehiko Hihara, Wei Zhang, and ZhengMing Sun**

Owing to the considerable capacity, high safety, and abundant zinc resources, zinc-ion batteries (ZIBs) have been garnering much attention. Nonetheless, the unsatisfactory cyclic lifespan and poor reversibility originate from side reactions and dendrite obstacles to their practical applications. In addition to inhibiting the corrosion of aqueous electrolytes, regulating planar deposition is a key strategy to enhance their long-term stability. Herein, an in situ conversion strategy is reported to construct a protective "dual-layer" structure (VZSe/V@Zn) on zinc metal, consisting of the VSe_2-ZnSe outer layer with low lattice mismatch to Zn (002) plane, and corrosion-resistant nanometallic V inner layer. Such design integrates superior interfacial ionic/electronic transfer, corrosion resistance, and unique planar deposition regulation capability. The as-prepared VZSe/V@Zn demonstrates remarkable durability of 238 h at 50 mA cm^{-2} with a high depth of discharge (68.3% DOD) in the Zn||Zn symmetric cell. Even in the anode-free system, the as-prepared protective layer can extend the cycle life up to 2000 cycles, with an outstanding capacity retention of 93.1% and ultra-high average coulombic efficiency of 99.998%. This work delineates an effective strategy for fabricating lattice-matching protective layers, with profound implications for elucidating zinc deposition mechanisms and paving the way for the development of high-performance zinc batteries.

1. Introduction

Aqueous zinc-ion batteries (ZIBs) are considered as the forefront of the next-generation energy supply paradigm, owing to their exceptional combination of impressive capacity (820 mAh g^{-1} and 5855 mAh cm^{-3}), elevated safety standards, and the abundant availability of zinc resources.[1–4] Nonetheless, the zinc anode suffers from inhomogeneous surface charge distribution and uncontrollable dendrite growth.[5–7] Besides, side reactions such as hydrogen evolution reaction (HER) and interfacial passivation at the anode/electrolyte interface may erode zinc anodes, ultimately causing rapid decay in coulomb efficiency and unsatisfactory interfacial charge transfer.[8,9] Therefore, regulating the interfacial zinc deposition and inhibiting the side reactions are of significant in enhancing the long-term cyclic stability of Zn anodes.[10–12]

Fabricating inert layers such as $CaCO_3$,[13] TiO_2[14] or MOFs[15] presents an effective strategy to impede corrosion and minimize side reactions by isolating the Zn anode from direct contact with water, while the sluggish diffusivity of Zn^{2+} at the anode/electrolyte interface may compromise interfacial ion transmission.[16,17] To improve ionic transportation, zincophilic coatings have been developed to reduce the interfacial energy barrier of the nucleation, such as ZnTe[18] or ZnP[19] interlayer, which could promote the zinc redox kinetics. Nonetheless, the "hostless" nature of the zinc anode results in infinite volume expansion, posing the risk of damaging the coating during random zinc plating.[20,21] Therefore, designing coatings that intrinsically regulate the behavior of zinc deposition to avoid coating damage and subsequent interfacial corrosion.

The behavior of zinc deposition is intricately linked to the atomic structure of its surface. Unlike other typical low-index facets of zinc anodes (100 and 101 planes), the (002) plane displays a highly ordered and relatively smooth surface, which imparts higher HER inhibition, lower surface energy, and smaller volume variations.[22–24] Consequently, this oriented deposition mitigates interfacial damage originating from the formation of zinc dendrites with a high Young's modulus.[25,26] To facilitate zinc planar deposition, the spontaneous adsorption and in situ bonding of polyaspartic acid on zinc anodes

H. Zhang, Y. You, T. Shui, W. Zhang, Z. Sun
School of Materials Science and Engineering
Southeast University
Nanjing 211189, China
E-mail: w69zhang@seu.edu.cn; zmsun@seu.edu.cn
D. Sha
School of Materials Science and Engineering
Yangzhou University
Yangzhou 225009, China
N. Moloto
Molecular Science Institute
School of Chemistry
University of the Witwatersrand
Private Bag 3, Wits 2050, South Africa
J. Liu, S.-Z. Kure-Chu, T. Hihara
Department of Materials Function and Design
Nagoya Institute of Technology
Gokiso-cho, Showa-ku, Nagoya, Aichi 4668555, Japan

The ORCID identification number(s) for the author(s) of this article can be found under https://doi.org/10.1002/adma.202409763

DOI: 10.1002/adma.202409763

 © 2024 Wiley-VCH GmbH

15214095, 2024, 44, Downloaded from https://advanced.onlinelibrary.wiley.com/doi/10.1002/adma.202409763 by University Of Witwatersrand, Wiley Online Library on [12/12/2024]. See the Terms and Conditions (https://onlinelibrary.wiley.com/terms-and-conditions) on Wiley Online Library for rules of use; OA articles are governed by the applicable Creative Commons License

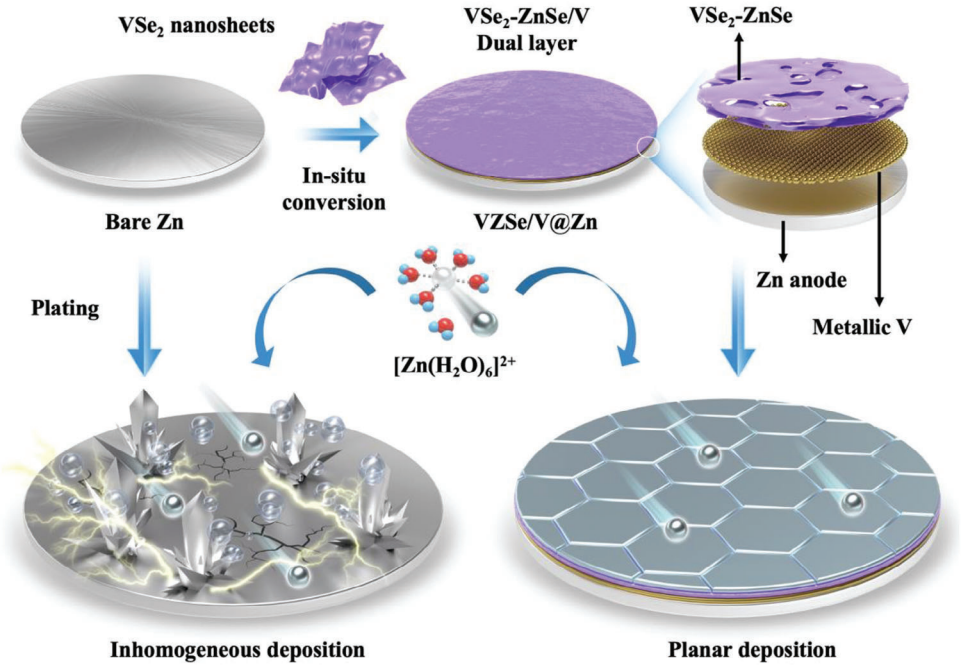


Figure 1. Schematic illustration of the in situ conversion engineering for constructing VZSe/V@Zn anode with a "dual-layer" structure, consisting of low lattice mismatch VSe_2-ZnSe outer layer and corrosion-resistant V inner layer, thus synergistically inducing planar zinc deposition.

have been developed, subsequently achieving dense and homogeneous (002) stacking.[27] However, uncontrollable macromolecular adsorption hinders the desolvation process of zinc ions, thereby compromising the durability of zinc plating/stripping at high discharge depths (DOD). Constructing nitrogen-doped graphene oxide[28] or vermiculite[29] substrates with intrinsic lattice-matching properties can promote planar deposition without increasing the interfacial desolvation energy barrier. However, the deposition process involves the usage of large amounts of binders (PVDF or PTFE, more than 10 wt%), which is detrimental to the homogenization of the electric field at the interface.[30,31] Therefore, it is highly desired to construct binder-free interfaces with strong interactions. Moreover, in pursuit of higher energy density, such as anode-free configuration, the requirement for reversibility in zinc deposition/stripping becomes more stringent.[32,33] Establishing interfaces that can simultaneously integrate planar deposition, corrosion resistance, and superior ionic/electronic transmission is imperative for enhancing zinc utilization.

Herein, we developed an in situ conversion strategy to construct a coupling structure on the zinc anode (VSe_2-ZnSe/V@Zn, VZSe/V@Zn) to achieve long-term stable and reversible planar deposition. The protective layer is chemically bonded to the zinc anode through an in situ interfacial solid-phase reaction, which simultaneously fabricates a "dual-layer" structure. The VSe_2-ZnSe hybrid outer layer possesses low lattice mismatch (δ) with Zn (002) plane, with a δ of 23.5% for VSe_2 (011) and 12.7% for ZnSe (111), and superior electronic conductivity (1150 S cm^{-1}), promoting ordered planar zinc growth. The nanometallic inner metallic V layer has great corrosion resistance properties, thus inhibiting electrolyte corrosion of the anode. Benefiting from such a "dual-layer" design, the as-prepared VZSe/V@Zn demonstrates notable plating/stripping reversibility in Zn||Zn symmetrical batteries even at an ultrahigh current density (238 h at 50 mA cm^{-2}) with 68.3% DOD, and a remarkable cumulative plating capacity (CPC) of 5.95 Ah cm^{-2}. Moreover, when paired with the ZnV_3O_8 cathode in an anode-free system, it maintains a remarkable cyclic lifespan in coin cells (2000 cycles), with 93.6% capacity retention and great reversibility (99.998% average coulombic efficiency). This work presents an effective approach to constructing lattice-matching protective layers, with potential implications for advancing the understanding of zinc deposition behavior and building high-performance zinc batteries.

2. Result and Discussion

The in situ construction process of the protective layer is illustrated in **Figure 1**. The 1T-VSe_2 nanosheets were uniformly distributed on the zinc anode via spray coating. After calcination in Ar atmosphere at 300 °C, the in situ conversion process occurred following Equation (1):

$$2Zn + VSe_2 \rightarrow 2ZnSe + V \quad (1)$$

The conventional in situ conversion strategy is limited to the phase transformation of the coating material itself and does not involve reaction with the zinc anode. Therefore, the use of binders is unavoidable, which adversely affects the electric field homogeneity and zincophilicity.[34,35] In contrast, this design reacts with the zinc anode, thus constructing a tight interaction that avoids the influence of the binder and promotes a homogeneous deposition of zinc at the interface. The heating process promotes the diffusive dissolution of Zn atoms at the interface and

 © 2024 Wiley-VCH GmbH

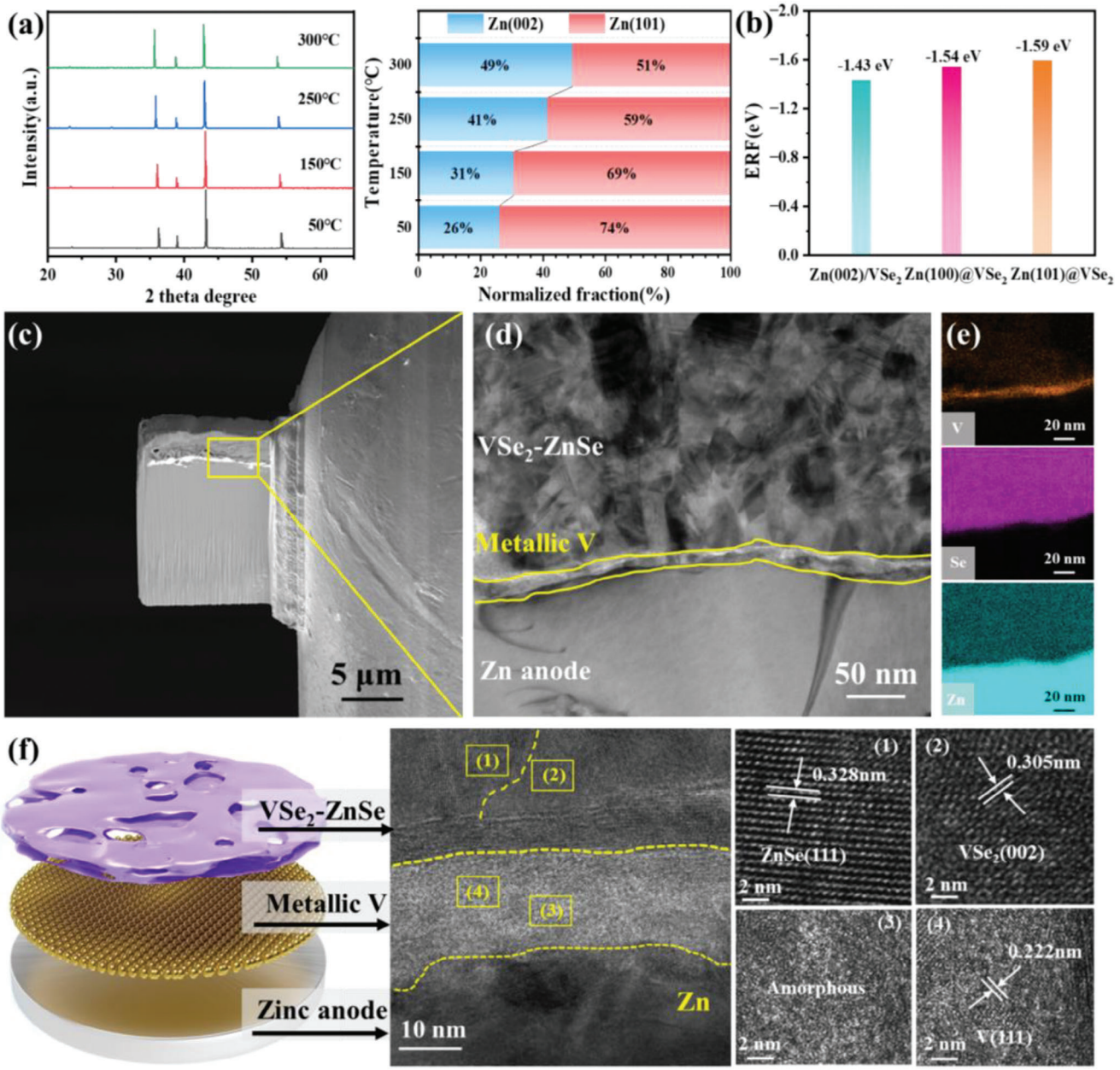


Figure 2. a) In situ XRD of the VZSe/V@Zn anode and the corresponding normalized fraction of the different Zn crystal planes. b) DFT simulation of the ERF between VSe_2 and different zinc anode crystal planes. c) Cross-sectional FIB-SEM image of the VZSe/V@Zn anode. d) TEM image of the VZSe/V@Zn anode and e) the corresponding elemental mapping. f) Schematic illustration of the "dual-layer" structure and the corresponding HRTEM images of the VZSe/V@Zn anode.

simultaneously provides sufficient energy for V-Se bond breaking, leading to the substitution of zinc and vanadium atoms at the interface.[35–37] However, prolonging the heating time will result in the total decomposition of VSe_2, resulting in a decrease in the interfacial conductivity from 1130 ± 11 to 105 ± 8 S cm^{-1} (Figure S1a, Supporting Information). Moreover, increasing the heating temperature above 400 °C causes the conductivity of the coating to drop drastically to 10^{-3} S cm^{-1} due to the fact that all of the VSe_2 is converted to ZnSe (Figure S1b, Supporting Information). In addition, the incompatibility between zinc and vanadium prevents the formation of stable intermetallic compounds.[38] As a result, vanadium atoms are enriched at the interface rather than inside the zinc lattice, forming a unique "dual-layer" structure, which consists of the VSe_2-ZnSe outer layer, and short-range ordered nanometallic vanadium inner layer. In situ XRD was performed to observe the formation process of the protective layer on the zinc anode. As the temperature increases, the Zn (101) crystallites preferentially react and decrease from 74% to 51%, exposing more Zn (002) crystallites (**Figure 2**a). The formation of ZnSe was also confirmed by the XRD results (Figure S2,

© 2024 Wiley-VCH GmbH

15214095, 2024, 44, Downloaded from https://advanced.onlinelibrary.wiley.com/doi/10.1002/adma.202409763 by University Of Witwatersrand, Wiley Online Library on [12/12/2024]. See the Terms and Conditions (https://onlinelibrary.wiley.com/terms-and-conditions) on Wiley Online Library for rules of use; OA articles are governed by the applicable Creative Commons License

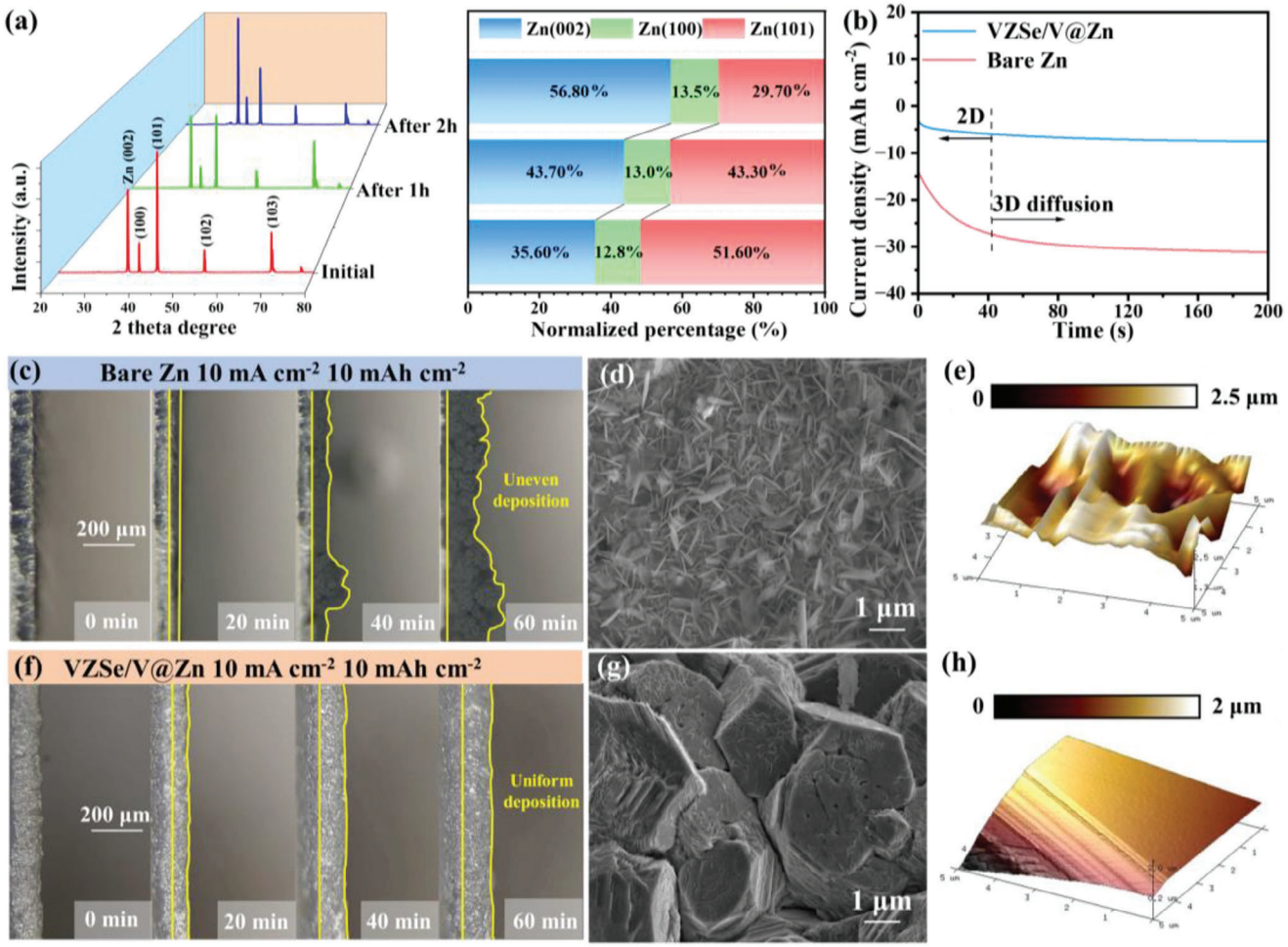


Figure 3. a) XRD pattern of the VZSe/V@Zn anode and h) corresponding $RCT_{(hkl)}$ of the different Zn crystal planes under 5 mA cm^{-2} deposition current density. b) CA curves of the bare Zn anode and the VZSe/V@Zn anode at a -150 mV overpotential. c) In situ optical microscopy image of the bare Zn anode, and d) the corresponding SEM image and e) AFM 3D reconstruction image after zinc plating. f) In situ optical microscopy image of the VZSe/V@Zn anode, and g) the corresponding SEM image and h) AFM 3D reconstruction image after zinc plating. Both samples are tested under 10 mA cm^{-2} current density and 10 mAh cm^{-2} cumulative plating capacity.

Supporting Information). Besides, the enthalpy of formation of reaction (ERF) between VSe_2 and various zinc anode low facet crystal planes was analyzed via DFT calculation, which is illustrated in Figure 2b. It can be seen that during the formation of the "dual-layer" structure, Zn (100) and (101) planes are more inclined to participate in the interfacial conversion reaction, which not only promotes the exposure of more (002) planes, but also builds more zincophilic sites, converting nonplanarly oriented zinc metal into ZnSe matching the Zn (002) planes, and therefore synergistically promotes planar deposition.

To characterize the structure of the as-prepared protective layer, the top-view morphology and the corresponding elemental mapping of the VZSe/V@Zn anode are shown in Figure S3 (Supporting Information), demonstrating a homogeneous coating on the surface of the Zn anode. The cross-sectional FIB-SEM image of the VZSe/V@Zn anode is illustrated in Figure 2c, revealing a significant linear contrast between the coating and the zinc substrate, indicating the formation of the "dual-layer" coating. Then the FIB-TEM image and corresponding elemental mapping of are shown in Figure 2d,e, demonstrating the enrichment of vanadium at the interface, consistent with the linear sweep result (Figure S3, Supporting Information). HRTEM results further confirm the formation of the "dual-layer" structure (Figure 2f), consisting of the VSe_2-ZnSe outer layer with low-lattice mismatch, and the metallic V inner layer with superior corrosion resistance, thereby synergistically promoting the planar deposition and enhancing the reversibility of the zinc plating/stripping.

To investigate the textural difference of the electrochemical deposition between the bare Zn and VZSe/V@Zn anode, the XRD results (**Figure 3a**) and the corresponding relative texture coefficient ($RTC_{(hkl)}$) were calculated based on the following equation (2):[39]

$$RTC_{(hkl)} = \frac{I_{hkl}/I^0_{hkl}}{\sum I_{hkl}/I^0_{hkl}} \times 100\% \quad (2)$$

© 2024 Wiley-VCH GmbH

15214095, 2024, 44, Downloaded from https://advanced.onlinelibrary.wiley.com/doi/10.1002/adma.202409763 by University Of Witwatersrand, Wiley Online Library on [12/12/2024]. See the Terms and Conditions (https://onlinelibrary.wiley.com/terms-and-conditions) on Wiley Online Library for rules of use; OA articles are governed by the applicable Creative Commons License

where I^0_{hkl} and I_{hkl} correspond to the intensities of the Zn before and after deposition, respectively. Compared to the bare Zn anode (Figure S5, Supporting Information), the $RTC_{(002)}$ value of VZSe/V@Zn anode exhibits a significant increase in oriented deposition, rising from 35.6% to 56.8%. Generally, when the $\Delta RTC_{(hkl)}$ value reaches 20%, the preferred orientation as (hkl) is evident.[40,41] The chronoamperometry (CA) test also examines Zn nucleation and growth behavior. As shown in Figure 3b, the current of the bare Zn sample continuously increases to more than 30 mA cm^{-2} throughout the process, indicating that Zn ions tend to aggregate or form dendrites to minimize surface energy, corresponding to 2D diffusion control.[42] In contrast, the VZSe/V@Zn sample reaches 7.2 mA cm^{-2} in less than 40 s and remains stable, indicating uniform nucleation and epitaxial crystal growth.

To visualize the zinc deposition behavior, in situ optical microscopy combined with SEM was employed. Both samples were deposited at 10 mA cm^{-2} with an areal capacity of 10 mAh cm^{-2}. The bare Zn anode shows inhomogeneous growth in cross-sectional view with the continuous increase of zinc deposition time (Figure 3c). The surface morphology after deposition illustrates irregular zinc arrangement and significant dendrite growth (Figure 3d and Figure S6a, Supporting Information). The AFM 2D image and corresponding 3D reconstruction morphology also exhibit the same results (Figure 3e and Figure S7a, Supporting Information). In comparison, the VZSe/V@Zn anode maintains uniform deposition throughout the reaction process (Figure 3f), Unlike customary inert coatings, conductive coatings allow zinc to be deposited on the coating.[28,43,44] Due to the low lattice mismatch of the as-prepared coating, it could act as a culture substrate to regulate the planar zinc deposition. Therefore, Zn platelets with a high fraction of (002) facets are observed (Figure 3g and Figure S6b, Supporting Information). Additionally, the corresponding AFM 2D and 3D morphology are shown in Figure 3h and Figure S7b (Supporting Information), demonstrating that the introduction of the as-prepared coating enables uniform planar zinc deposition. The post-cycling XRD results of the different samples are shown in Figure S8 (Supporting Information). In the bare zinc sample, a distinct characteristic peak was observed at 8°, corresponding to the (001) plane of the zinc hydroxide sulfate (ZHS).[45,46] In contrast, the VZSe/V@Zn sample exhibits no diffraction peaks of the ZHS, indicating that the coating inhibits the side-reactions, thereby reducing the by-products. To investigate the effect of the introduction of coatings on the surface nucleation, the surface energy of different surfaces was evaluated using the Good and van Oss model[47] as shown in the following Equation (3):

$$\gamma = \gamma^{LW} + \gamma^{AB} = \gamma^{LW} + 2\sqrt{\gamma^{+}\gamma^{-}} \quad (3)$$

where γ^{LW} and γ^{AB} correspond to the apolar Lifshitz-van der Waals interactions and the polar Lewis-acid/base interactions (electron-donor parameter γ^{-} and electron-acceptor parameter γ^{+}). And the three-probe-liquid contact angle measurement was utilized to calculate the surface energy of the different solid surface,[48] as presented in Equation (4) below:

$$\gamma(1+\cos\theta) = 2\sqrt{\gamma_S^{LW}\gamma_L^{LW}} + = 2\sqrt{\gamma_S^{+}\gamma_L^{-}} + 2\sqrt{\gamma_S^{-}\gamma_L^{+}} \quad (4)$$

where θ corresponds to the contact angel of the liquid, L and S represent the corresponding parameters of solid and liquid. Here, three typical liquids with known parameters were employed (Table S1, Supporting Information), and the contact angles of different samples with different liquids are listed in Table S2 (Supporting Information).

Therefore, the total surface energies of coated and bare zinc anodes were calculated according to Equation 4 above, which has been listed in Table S3 (Supporting Information), indicating that the introduction of the coating could reduce the surface energy from 45.98 to 41,48 kJ m^{-2}, thereby promoting the nucleation process.

DFT calculations were performed to analyze the mechanism by which the protective layer promotes stable deposition at the interface. The atomic structure of the VZSe/V@Zn is illustrated in **Figure** 4a. The unbalanced charge distribution confirms the tightly bonding between the Zn anode and protective layer.[49] As shown in Figure 4b, the interfacial transport capability for zinc ions was compared between the spontaneous generation of zinc hydroxide sulfate (ZHS) on the surface and the introduction of the protective layer. The VZSe/V@Zn demonstrates stronger interfacial charge transfer (0.285 e) compared to ZHS@Zn (0.21 e), indicating that the "dual-layer" design accelerates the Zn^{2+} diffusion at the interface.[50] The Total density of states (TDOS) of the VZSe/V@Zn and ZHS@Zn are exhibited in Figure 4c, confirming that VZSe/V is a good conductor of electrons compared to ZHS, thus serving as a substrate for directed growth cultures of zinc anodes. Additionally, the diffusion energy barriers of Zn^{2+} along the interface of VZSe/V@Zn and ZHS@Zn are compared in Figure 4d, demonstrating that the VZSe/V@Zn possesses a smaller energy barrier (0.21 eV) than ZHS@Zn (1.04 eV). The low diffusion energy barrier favors rapid Zn^{2+} transport and uniform ion distribution, thus enhancing its plating/stripping stability at a large current density.[51] The dendrite inhibition at the interface was also analyzed with the aid of Young's modulus (γ) and interfacial energy (E). Larger γ and E values could better avoid zinc aggregation and dendrite formation.[52] As shown in Table S4 (Supporting Information) and Figure 4e, the VZSe/V@Zn exhibits interfacial energy of 1.603 eV $Å^{-2}$ and a high Young's modulus of 99.1 GPa, while the ZHS@Zn only yields a low Young's modulus of 65 GPa and interfacial energy of 0.4602 eV $Å^{-2}$, suggesting that the as-prepared protective layer possesses superior mechanical property, thereby inhibiting the severe dendrite growth. Meanwhile, the H adsorption ability of the different interfaces was validated by the free energy (ΔG),[53] as shown in Figure 4f. The ΔG of VZSe/V@Zn (5.52 eV) is much higher than ZHS@Zn (2.88 eV), suggesting that the VZSe/V@Zn possesses stronger inhibition of H_2 evolution.

Benefiting from the planar deposition behavior, the as-prepared anode exhibits considerable zinc deposition/stripping reversibility and stability in the long-term cycles, which was further investigated in Zn||Zn symmetric batteries. To determine the optimal mass loading of the coating, the Zn||Zn symmetric cells were utilized to evaluate its performance. The rate performance of the VZSe/V@Zn with various coating mass ratios is shown in Figure S9 (Supporting Information), indicating that the optimal mass ratio is approximately 1 mg cm^{-2}. Consequently, this mass loading was employed for all subsequent performance evaluations. The polarization curves of the bare Zn

© 2024 Wiley-VCH GmbH

15214095, 2024, 44, Downloaded from https://advanced.onlinelibrary.wiley.com/doi/10.1002/adma.202409763 by University Of Witwatersrand, Wiley Online Library on [12/12/2024]. See the Terms and Conditions (https://onlinelibrary.wiley.com/terms-and-conditions) on Wiley Online Library for rules of use; OA articles are governed by the applicable Creative Commons License

15214095, 2024, 44, Downloaded from https://advanced.onlinelibrary.wiley.com/doi/10.1002/adma.202409763 by University Of Witwatersrand, Wiley Online Library on [12/12/2024]. See the Terms and Conditions (https://onlinelibrary.wiley.com/terms-and-conditions) on Wiley Online Library for rules of use; OA articles are governed by the applicable Creative Commons License

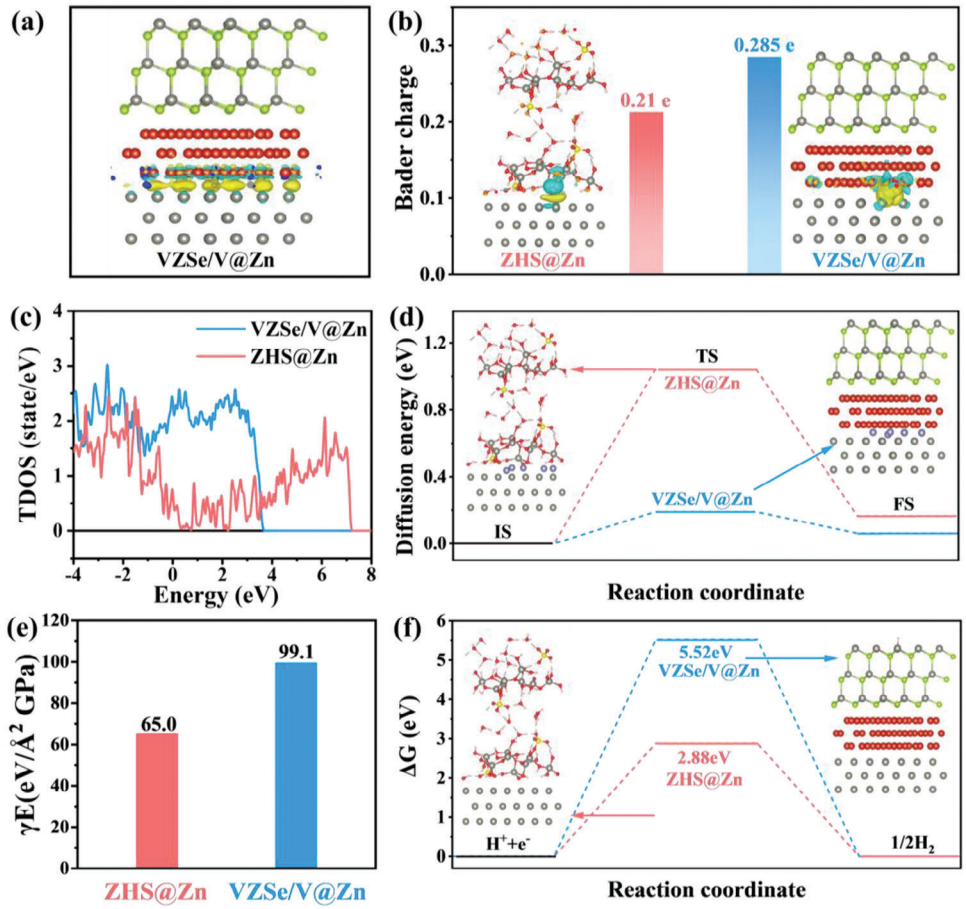


Figure 4. a) Electron density difference maps between VZSe/V and Zn. b) Electron density difference maps at the interfaces of VZSe/V@Zn and ZHS@Zn, and corresponding charge density differences and electron donations on these interfaces. c) The total density of states (TDOS) of the VZSe/V@Zn and ZHS@Zn. d) Diffusion pathways and energy barriers of Zn^{2+} at the interfaces in VZSe/V@Zn and ZHS@Zn. e) Zn-dendrite suppression ability (γE) and f) the free-energy diagram on the different surfaces for HER.

and VZSe/V@Zn anodes are shown in **Figure** 5a, demonstrating that the VZSe/V@Zn anode has a lower nucleation overpotential (NOP) compared to the bare Zn anode (14 mV vs 47 mV). This indicates that the design of the protective layer facilitates ion transfer and promotes nucleation, resulting in uniform zinc deposition. Additionally, the as-prepared protective layer shows preferred anti-corrosion properties and enhanced reaction kinetics, evaluated by linear scanning voltammetry (Figure 5b). Compared to bare Zn (−1.53 V vs Ag/AgCl), the VZSe/V@Zn anode exhibits a significant negative shift in the HER onset potential (−1.69 V vs Ag/AgCl). To further confirm the corrosion resistance of the "dual-layer" design, the $ZnSe/VSe_2$ hybrid single-layer coating was prepared via the mechanical mixing method. Their Tafel plots were illustrated in Figure 5c, suggesting that the VSe/ZnSe@Zn may increase the corrosion current from 1.33 to 2.26 mA cm^{-2}. This phenomenon can be attributed to the HER activity of VSe_2. In contrast, the introduction of the V layer can reduce the corrosion current to 0.81 mA cm^{-2}, indicating that the V layer can inhibit the HER, thus enhancing the reversibility of the zinc plating/stripping (Figure 5c). Benefiting from the integration of uniform deposition and anti-corrosion properties, the VZSe/V@Zn anode demonstrates remarkable durability at an ultra-high current density of 50 mA cm^{-2}, with a relatively low polarization potential (≈230 mV, Figure 5d). In addition, it shows an exceptional long-term cycle life of 2200 h at 1 mA cm^{-2} (Figure S10, Supporting Information), which is 22 times longer than that of bare zinc anodes. Even at 20 and 50 mA cm^{-2}, it maintains reversible plating/stripping for 650 h and 238 h with 68.3% DOD (Figure 5e,f). Compared with the previous reports (Table S5, Supporting Information), the as-prepared VZSe/V@Zn anode exhibits an ultra-high cumulative plating capacity (CPC) of 6.5 and 5.95 Ah cm^{-2} at 20 and 50 mA cm^{-2}, respectively (Figure 5g). Compared with the inert coatings such as Nano Si or ZPO, Our design promotes planar zinc deposition for superior CPC at higher current densities.

To evaluate the performance of the VZSe/V@Zn anode in full cells, a coin cell system was employed for conventional electrochemical evaluations. The Ammonium vanadate ($NH_4V_4O_{10}$, NVO), synthesized via a conventional hydrothermal process, was employed as a cathode (Figure S12, Supporting Information). The CV curves of the full cells are shown in **Figure** 6a. Compared to the bare Zn||NVO full cell, the VZSe/V@Zn||NVO full cell demonstrates lower polarization and a higher platform capacity contribution. The Nyquist plots of the full cells

 © 2024 Wiley-VCH GmbH

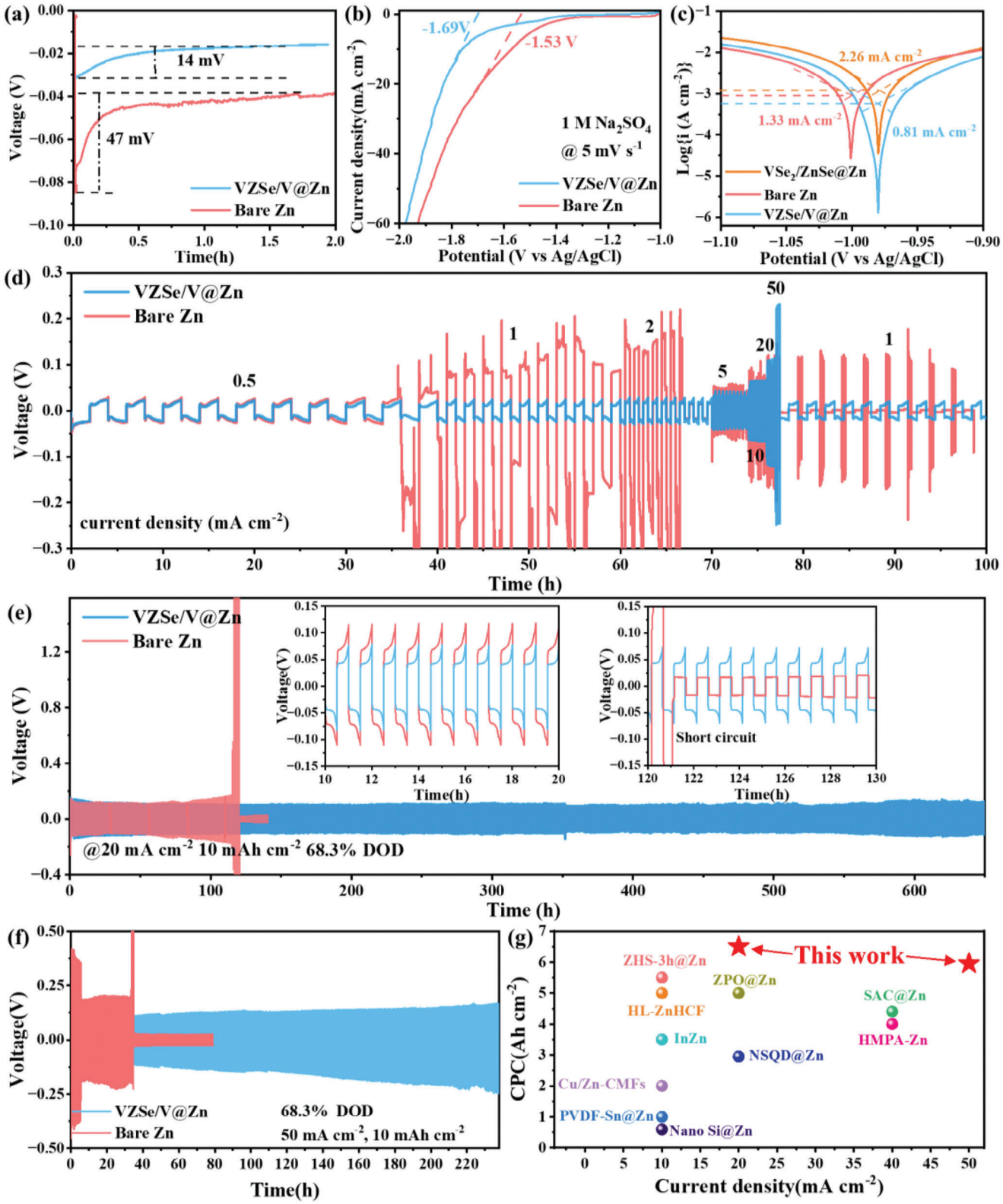


Figure 5. a) Nucleation overpotential, b) LSV curve and c) Tafel plots of the VSe_2/ZnSe@Zn, VZSe/V@Zn and bare Zn anode. d) Rate performance of VZSe/V@Zn anode and bare Zn anode from 0.5 to 50 mA cm^{-2}. Long-term cyclic performance of VZSe/V@Zn anode and bare Zn anode at e) 20 and f) 50 mA cm^{-2}, respectively, with an areal capacity of 10 mAh cm^{-2}. g) The CPC comparison of the Zn symmetric cell using VZSe/V protective layer with other reported literatures.

© 2024 Wiley-VCH GmbH

15214095, 2024, 44, Downloaded from https://advanced.onlinelibrary.wiley.com/doi/10.1002/adma.202409763 by University Of Witwatersrand, Wiley Online Library on [12/12/2024]. See the Terms and Conditions (https://onlinelibrary.wiley.com/terms-and-conditions) on Wiley Online Library for rules of use; OA articles are governed by the applicable Creative Commons License

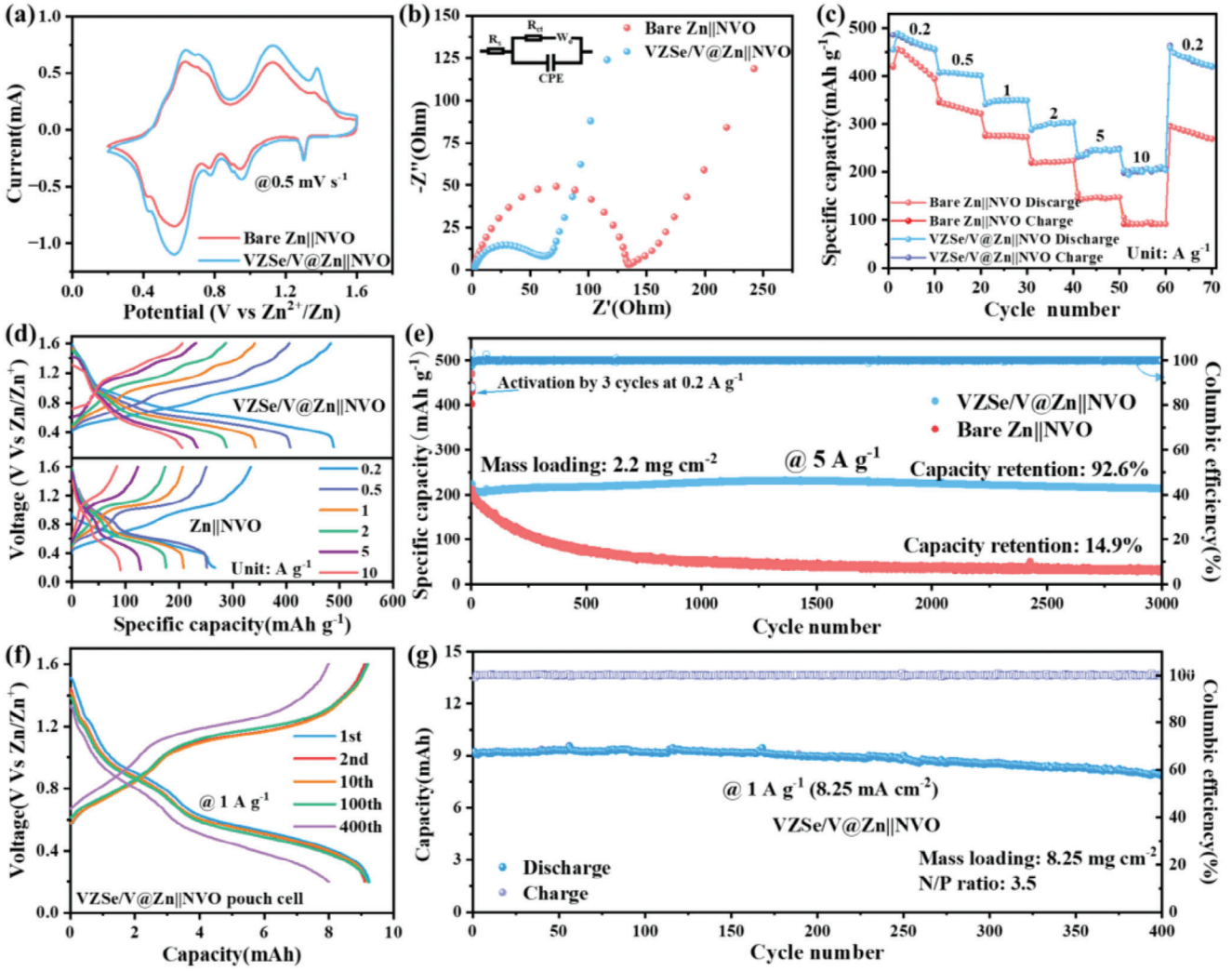


Figure 6. a) CV curves and b) Nyquist plots of the VZSe/V@Zn||NVO and the bare Zn||NVO full cells. c) Rate capability and d) corresponding Charge/discharge profiles of the VZSe/V@Zn||NVO and the bare Zn||NVO full cells from 0.2 to 10 A g^{-1}. e) Long-term cycling performance of the VZSe/V@Zn||NVO and the bare Zn||NVO full cells at 5 A g^{-1}. f) Charge/discharge profiles of the VZSe/V@Zn||NVO pouch cells and g) long-term cycling performance of the VZSe/V@Zn||NVO pouch cells at 1 A g^{-1}.

and the corresponding equivalent circuit diagram (Figure 6b) show that the VZSe/V@Zn||NVO full cell possesses a lower interfacial charge transfer impedance (67.8 Ω) compared with bare Zn||NVO full cell (133.6 Ω), indicating the introduction of the VZSe/V protective layer enhances charge transfer and facilitates ion diffusion. Additionally, the VZSe/V@Zn||NVO full cell exhibits superior rate capability, delivering capacities of 485, 407, 343, 290, 234, and 206 mAh g^{-1} at 0.2, 0.5, 1, 2, 5, and 10 A g^{-1}, respectively, outperforming the bare Zn||NVO full cells (Figure 6c,d). Additionally, the VZSe/V@Zn||NVO full cell demonstrates a remarkable cyclic lifespan, with a capacity of 214.6 mAh g^{-1} at 5 A g^{-1} after 3000 cycles, achieving 92.6% capacity retention. In contrast, the bare Zn||NVO full cell only delivers a capacity of 64.2 mAh g^{-1} under the same conditions (28.7% capacity retention). Furthermore, the cyclic performance of the VZSe/V@Zn||NVO pouch cell with a high mass loading (8.25 mg cm^{-2}) is shown in Figure 6f. It delivers a capacity of 8.2 mAh with 90.3% capacity retention after 400 cycles at 1 A g^{-1} and can power a thermohydrometer (Figure S13, Supporting Information), demonstrating its potential for practical applications.

To evaluate the feasibility of the as-prepared protective layer in the anode-free configuration, the protective layer was prepared on a copper substrate. Before spraying and calcination treatment, a nominal amount of zinc was pre-plated to create the same interfacial reaction environment (see the experimental section for details). Since the in situ conversion could consume the VSe_2, and the electrochemical window cannot match the demand, the capacity contribution of the VSe_2 can be neglected.[54,55] Compared with conventional zinc batteries, anode-free systems enhance energy density by avoiding the use of excess zinc metal.[56] However, without excess zinc compensation, the cycle lifespan decays more rapidly, demanding higher reversibility of zinc deposition and stripping (**Figure 7a**). The cyclic reversibility of VZSe/V@Cu was evaluated by the average coulombic efficiency (ACE), which was investigated using Zn||Cu half-cells. The VZSe/V@Cu

© 2024 Wiley-VCH GmbH

15214095, 2024, 44, Downloaded from https://advanced.onlinelibrary.wiley.com/doi/10.1002/adma.202409763 by University Of Witwatersrand, Wiley Online Library on [12/12/2024]. See the Terms and Conditions (https://onlinelibrary.wiley.com/terms-and-conditions) on Wiley Online Library for rules of use; OA articles are governed by the applicable Creative Commons License

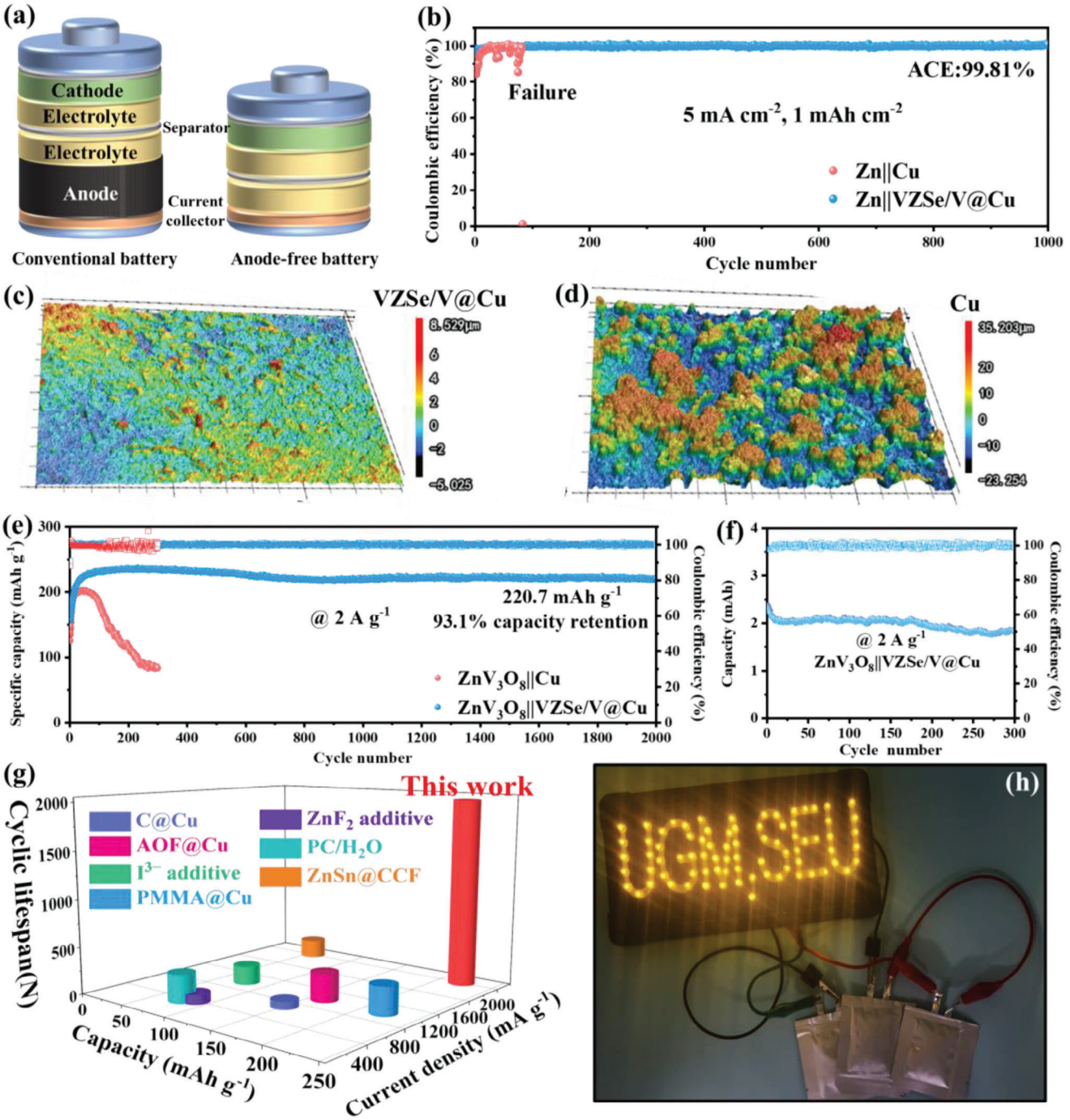


Figure 7. a) Schematic illustration of the conventional zinc battery and anode-free battery. b) Cyclic performance of the Zn||VZSe/V@Cu and Zn||bare Cu half cells. CLSM of the c) VZSe/V@Cu and d) bare Cu after deposition at 5 mA cm^{-2}. e) Cyclic performance of the ZnV_3O_8||VZSe/V@Cu and the ZnV_3O_8|| bare Cu coin cells at 2 A g^{-1}. f) Cyclic performance of the ZnV_3O_8||VZSe/V@Cu pouch cell at 2 A g^{-1}. g) Comparison of cycle life of Cu||ZnV_3O_8 full cells using VZSe/V@Cu with the reported anode-free zinc batteries. h) Photograph of the VZSe/V@Cu||ZnV_3O_8 pouch cells powering LED lights (3.2 V).

exhibited an ACE of 99.81% after 1000 cycles at 5 mA cm^{-2}, while bare Cu only achieved a poor cyclic life of 85 cycles and a relatively low ACE of 97% (Figure 7b). The morphology of different current collectors after deposition was observed by a confocal laser scanning microscope (CLSM, Figure 7c,d). VZSe/V@Cu demonstrated more uniform deposition, smaller and denser nucleated grains, and smaller height differences compared to bare Cu.

The VZSe/V@Cu was assembled with the ZnV_3O_8 cathode to evaluate its electrochemical performance. The cyclic performance of the ZnV_3O_8||VZSe/V@Cu full-cell is shown in

© 2024 Wiley-VCH GmbH

15214095, 2024, 44, Downloaded from https://advanced.onlinelibrary.wiley.com/doi/10.1002/adma.202409763 by University Of Witwatersrand, Wiley Online Library on [12/12/2024]. See the Terms and Conditions (https://onlinelibrary.wiley.com/terms-and-conditions) on Wiley Online Library for rules of use; OA articles are governed by the applicable Creative Commons License

Figure 7e, delivering a capacity of 220.7 mAh g^{-1} after 2000 cycles, with a high ACE of 99.998% and 93.1% capacity retention. In contrast, the ZnV_3O_8||bare Cu full-cell maintained fewer than 100 reversible cycles and failed after 300 cycles. Compared with other strategies for constructing high-performance anode-free zinc batteries, our design demonstrates the best cyclic lifespan and capacity, with remarkable capacity retention and high average coulombic efficiency (Figure 7g and Table S6, Supporting Information). The rate performance of the different anode-free full cell samples is shown in Figure S14 (Supporting Information), where the ZnV_3O_8||VZSe/V@Cu full cell exhibited twice the specific capacity and superior capacity retention. Furthermore, ZnV_3O_8||VZSe/V@Cu pouch cells were assembled, delivering a capacity of 1.9 mAh after 300 cycles, with an energy density of 41.6 Wh kg^{-1} (Figure 7f), and can power the LED lights (Figure 7h). These results demonstrate the feasibility of the protective layer for enhancing the cyclic lifespan of anode-free zinc batteries.

3. Conclusions

In summary, we developed an in situ conversion strategy to construct a "dual-layer" protective structure on zinc anode, consisting of low lattice mismatch VSe_2-ZnSe outer layer and corrosion-resistant nanometallic V inner layer, facilitating planar deposition and enhancing the reversibility of the zinc plating/stripping. The VZSe/V@Zn demonstrated considerable durability during symmetric cell evaluation (238 h at 50 mA cm^{-2}) with a high CPC (5.95 Ah cm^{-2}). Furthermore, when utilized in full cells with NVO cathode, it exhibited a remarkable cyclic lifespan (8.2 mAh after 400 cycles at 1 A g^{-1}, with 90.3% capacity retention). Even in an anode-free system, it showed impressive cyclability, which maintains 93.1% capacity retention after 2000 cycles at 2 A g^{-1} with an ACE of 99.998%. This work not only demonstrates a facile strategy for fabricating a protective layer with lattice matching and corrosion-resistant properties but also provides advanced sightseeing for understanding zinc deposition behavior and building high-performance zinc batteries.

4. Experimental Section

Materials: Vanadyl acetylacetonate ($VO(Ac)_2$, 98%, Aladdin), selenium powder (Se, 99.99%), zinc sulfate ($ZnSO_4{\cdot}7H_2O$), oleyl amine (80–90%) and hexane (99%) were purchased from Shanghai Aladdin Co. Ltd. Zinc foil (99.99%), Ti foil (10 µm) and Cu foil (7 µm) were purchased from Chengshuo Metal Materials Co., Ltd. The additives, including Super P and PVDF were purchased from Nanjing Mojiesi Energy Technology Co., Ltd.

Preparation of the VSe_2 Precursor: The synthesis of the VSe_2 nanosheets is according to the previous reports.[57] Typically, 5.4 mmol $VO(Ac)_2$ and 10.8 mmol Se powder were slowly added into 180 mL oleyl amine and kept stirring for 6 h at 330 °C. The reaction was carried out under an Ar atmosphere. Next, the products were washed with the hexane several times and dried in a vacuum oven for 12 h at 80 °C. Finally, the VSe_2 nanosheets were obtained after calcination at 500 °C in Ar atmosphere for 3 h.

Preparation of the VZSe/V@Zn and VZSe/V@Cu: The VZSe/V@Zn was prepared via conventional spray coating. Generally, 100 mg VSe_2 nanosheets were dispersed into 20 mL ethanol and kept ultrasonicating for 10 min. Then the as-prepared colloidal suspension was sprayed on the zinc foil at 80 °C with a mass loading of ≈1.0 mg cm^{-2}. Finally, the VZSe/V@Zn was obtained after calcination at 300 °C in the Ar atmosphere for 1.5 h.

Before the fabrication of VZSe/V@Cu, 0.5 mg cm^{-2} of zinc (≈0.41 mAh cm^{-2}) needs to be preplated on the Cu foil at 0.5 mA cm^{-2}, and the subsequent steps are the same as the abovementioned.

General Characterization and In Situ Observations: The chemical compositions were observed by the Haoyuan DX-2700b X-ray diffraction (XRD, Liaoning, China) combined with MDI JADE software and Thermofisher 4800 X-ray photoelectron spectroscopy (XPS, U.S.A). The morphology was observed by Crossbeam350 FIB scanning electron microscope (SEM, Zeiss, Germany), Talos F200X transmission electron microscope (TEM, Thermofisher, USA), and Dimension ICON atomic force microscope (AFM, Bruker, USA).

The in situ XRD was observed by SmartLab SE (Rigaku, Japan), which is heated at 2 °C per minute and conducted at Ar atmosphere. The in situ electrochemical deposition was observed by the Zeiss optical microscope combined with an electrochemical workstation (Biological SP-150, France). The orientation of electrodeposited zinc was influenced by the anisotropy of the substrates, which can be evaluated by the lattice mismatch (δ) between the Zn (002) plane and the coating according to Equations (5) and (6) below:[29,40.58–60]

$$\delta = \left| \frac{d_{substrate} - d_{Zn(002)}}{d_{Zn(002)}} \right| \times 100\% \; d_{substrate} < 1.5 d_{Zn(002)} \tag{5}$$

$$\delta = \left| \frac{d_{substrate} - 2d_{Zn(002)}}{d_{Zn(002)}} \right| \times 100\% \; 1.5 d_{Zn(002)} < d_{substrate} < 2.5 d_{Zn(002)} \tag{6}$$

where $d_{substrate}$ and $d_{Zn(002)}$ correspond to the respective crystal plane spacing. The contact interface can be divided into incoherent (δ > 25%) semicoherent (25%> δ >5%) and coherent interfaces (δ < 5%). Then based on the equation above, the δ of VSe_2 and ZnSe is 23.5% and 12.7%, respectively.

Electrochemical Test: CR2032-type coin cells were employed for the fundamental electrochemical performance evaluations. For the symmetric cells, Zn||Zn anodes and VZSe/V@Zn||VZSe/V@Zn anodes were assembled with 2 M Zinc sulfate ($ZnSO_4{\cdot}7H_2O$) electrolyte and glass fiber separator (Whatman GF/D) in an open environment. The depth of discharge (DOD) was calculated via Equation (7) above:[61]

$$\mathrm{DOD} = \frac{It}{V\nu} \times 100\% \tag{7}$$

where I correspond to the applied current density (mA cm^{-2}), t is the discharge time (h), ν is the volume of the Zn anode (cm^3), and V (mAh cm^{-3}) is the theoretical specific capacity of Zn (5855 mAh cm^{-3}).

For the full cells, the $NH_4V_4O_{10}$ (NVO) was synthesized to use as the cathode material according to the previous report.[62] The cathode was fabricated by the conventional doctor-blading method, which mixed the NVO, super P, and PVDF with a mass ratio of 7:2:1. while the other components are the same as the symmetric cells. The galvanostatic discharge–charge performance was monitored by the LAND CT-3001A test instrument, and the cyclic voltammetry (CV) and electrochemical impedance spectroscopy (EIS) were tested by the Biological SP-150 electrochemical workstation. The linear scanning voltammetry (LSV) and Tafel plots tests were analyzed by assembling a three-electrode system.

For the pouch cells, the area of both electrodes is 2 × 2.5 cm^2, while the NVO cathode was coated on the Ti foils with a mass loading of ≈8.25 mg cm^{-2}, and the electrochemical test was the same as the coin-cell tests. For the anode-free cell evaluations, the zinc anode was replaced by Cu and VZSe/V@Cu. And the ZnV_3O_8 was utilized as the cathode. All the tests are the same as the conventional zinc batteries mentioned above.

Computational Methods: The density functional theory (DFT) based first-principles calculations were carried out by the Vienna Ab initio

© 2024 Wiley-VCH GmbH

15214095, 2024, 44, Downloaded from https://advanced.onlinelibrary.wiley.com/doi/10.1002/adma.202409763 by University Of Witwatersrand, Wiley Online Library on [12/12/2024]. See the Terms and Conditions (https://onlinelibrary.wiley.com/terms-and-conditions) on Wiley Online Library for rules of use; OA articles are governed by the applicable Creative Commons License

Simulation Package (VASP) code[63] with the projector-augmented wave (PAW) pseudopotential. The Perdew-Burke-Ernzerhof (PBE)[64] generalized gradient approximation (GGA)[65] was performed to address the exchange and correlation effects. A cutoff energy of 500 eV was used for the electron-wave functions and the k mesh of 3×3×1 was adopted. The energy convergence step is set as 10^{-7} eV. The maximum Hellmann-Feyman force after ionic relaxation is less than 0.005 eV $Å^{-1}$ on each atom. A vacuum thickness of over 20 Å was added in the z direction to avoid unphysical interactions between periodic images. The long-range van der Waals interaction is incorporated by adopting the zero damping DFT-D3 method of Grimme.[66] The nudged elastic band (NEB) method is utilized to determine the diffusion energy barriers.[67] The Gibbs free energy at temperature T for each state was calculated by $G(T) = E_{DFT} + G_{correct}(T) = E_{DFT} + ZPE - TS + \Delta U_{0\rightarrow T}$, where $G_{correct}(T)$ is the thermal correction to the Gibbs free energy, ZPE is the zero-point energy, and $\Delta U_{0\rightarrow T}$ is internal energy change induced by temperature, respectively.

Supporting Information

Supporting Information is available from the Wiley Online Library or from the author.

Acknowledgements

H.Z. and Y.Y. contributed equally to this work. This work was supported by the National Key Research and Development Program of China (No. 2023YFC3009502), the National Natural Science Foundation of China (No. 52371134, U23A20574), Natural Science Foundation of Jiangsu Province (No. BK20231432), Aeronautical Science Foundation of China (2023Z015069001), the Fundamental Research Funds for the Central Universities (No. 2242023K40027) and the SEU Innovation Capability Enhancement Plan for Doctoral Students (CXJH_SEU 24151).

Conflict of Interest

The authors declare no conflict of interest.

Data Availability Statement

Research data are not shared.

Keywords

anode-free zinc batteries, in situ conversion, lattice matching, planar deposition

Received: July 8, 2024
Revised: August 12, 2024
Published online: August 30, 2024

[1] Y. Liang, H. Dong, D. Aurbach, Y. Yao, *Nat. Energy* **2020**, *5*, 646.
[2] Z. Yi, G. Chen, F. Hou, L. Wang, J. Liang, *Adv. Energy Mater.* **2021**, *11*, 2003065.
[3] J. Yang, R. Zhao, Y. Wang, Z. Hu, Y. Wang, A. Zhang, C. Wu, Y. Bai, *Adv. Funct. Mater.* **2023**, *33*, 2213510.
[4] W. Du, E. H. Ang, Y. Yang, Y. Zhang, M. Ye, C. C. Li, *Energy Environ. Sci.* **2020**, *13*, 3330.
[5] Q. Yang, Q. Li, Z. X. Liu, D. H. Wang, Y. Guo, X. L. Li, Y. C. Tang, H. F. Li, B. B. Dong, C. Y. Zhi, *Adv. Mater.* **2020**, *32*, 2001854.
[6] X. Yu, Z. Li, X. Wu, H. Zhang, Q. Zhao, H. Liang, H. Wang, D. Chao, F. Wang, Y. Qiao, H. Zhou, S. G. Sun, *Joule* **2023**, *7*, 1145.
[7] Q. Hu, J. Hou, Y. Liu, L. Li, Q. Ran, J. Mao, X. Liu, J. Zhao, H. Pang, *Adv. Mater.* **2023**, *35*, 2303336.
[8] J. Chen, W. Zhao, J. Jiang, X. Zhao, S. Zheng, Z. Pan, X. Yang, *Energy Storage Mater.* **2023**, *59*, 102767.
[9] J. Zheng, X. Liu, Y. Zheng, A. N. Gandi, X. Kuai, Z. Wang, Y. Zhu, Z. Zhuang, H. Liang, *Nano Lett.* **2023**, *23*, 6156.
[10] H. N. Zhang, W. Zhang, D. Luo, S. Y. Zhang, L. Q. Kong, H. Xia, Q. Xie, G. Xu, Z. W. Chen, Z. M. Sun, *Adv. Mater.* **2024**, *36*, 2401234.
[11] H. Xia, G. Xu, X. Cao, C. Y. Miao, H. N. Zhang, P. Y. Chen, Y. Zhou, W. Zhang, Z. M. Sun, *Adv. Mater.* **2023**, *35*, 2301996.
[12] H. Zhang, T. Shui, W. Zhang, Z. Sun, *Energy Storage Mater.* **2024**, *71*, 103595.
[13] L. Kang, M. Cui, F. Jiang, Y. Gao, H. Luo, J. Liu, W. Liang, C. Zhi, *Adv. Energy Mater.* **2018**, *8*, 1801090.
[14] Q. Zhang, J. Y. Luan, X. B. Huang, Q. Wang, D. Sun, Y. G. Tang, X. B. Ji, H. Y. Wang, *Nat. Commun.* **2020**, *11*, 3961.
[15] R. C. Zhang, Y. Feng, Y. X. Ni, B. D. Zhong, M. Y. Peng, T. J. Sun, S. Chen, H. Wang, Z. L. Tao, K. Zhang, *Angew. Chem., Int. Ed.* **2023**, *62*, 2304503.
[16] J. Hao, B. Li, X. Li, X. Zeng, S. Zhang, F. Yang, S. Liu, D. Li, C. Wu, Z. Guo, *Adv. Mater.* **2020**, *32*, 2003021.
[17] D. Deng, K. Fu, R. H. Yu, J. Zhu, H. W. Cai, X. C. Zhang, J. S. Wu, W. Luo, L. Q. Mai, *Adv. Mater.* **2023**, *35*, 2302353.
[18] D. W. Sha, C. J. Lu, R. X. Hu, Z. H. Bao, L. Pan, Z. M. Sun, *Energy Storage Mater.* **2024**, *66*, 103228.
[19] P. H. Cao, X. Y. Zhou, A. R. Wei, Q. Meng, H. Ye, W. P. Liu, J. J. Tang, J. Yang, *Adv. Funct. Mater.* **2021**, *31*, 2100398.
[20] Y. Gong, B. Wang, H. Ren, D. Li, D. Wang, H. Liu, S. Dou, *Nano-Micro Lett.* **2023**, *15*, 208.
[21] H. Yan, S. Li, J. Zhong, B. Li, *Nano-Micro Lett.* **2024**, *16*, 15.
[22] M. Li, C. Lai, X. He, Z. Zhang, J. Hu, B. Shan, K. Jiang, K. Wang, *ACS Appl. Mater. Interfaces* **2022**, *14*, 49719.
[23] Y. Lu, T. Wang, Z. Li, H. Cheng, K. Peng, Z. Tian, *Chem. Eng. J.* **2023**, *458*, 141509.
[24] M. Zhou, S. Guo, J. Li, X. Luo, Z. Liu, T. Zhang, X. Cao, M. Long, B. Lu, A. Pan, G. Fang, J. Zhou, S. Liang, *Adv. Mater.* **2021**, *33*, 2100187.
[25] W. Yuan, X. Nie, G. Ma, M. Liu, Y. Wang, S. Shen, N. Zhang, *Angew. Chem., Int. Ed.* **2023**, *62*, 2218386.
[26] Z. B. Chen, J. Zhao, Q. He, M. S. Li, S. Feng, Y. Z. Wang, D. Yuan, J. Y. Chen, H. S. Alshareef, Y. W. Ma, *ACS Energy Lett.* **2022**, *7*, 3564.
[27] T. Y. Zhou, Y. L. Mu, L. Chen, D. X. Li, W. Liu, C. K. Yang, S. B. Zhang, Q. Wang, P. Jiang, G. L. Ge, H. H. Zhou, *Energy Storage Mater.* **2022**, *45*, 777.
[28] L. A. Archer, K. J. Takeuchi, D. C. Bock, L. Wang, Y. Deng, X. Liu, G. D. Renderos, C. D. Quilty, J. Yin, T. Tang, Q. Zhao, J. Zheng, A. C. Marschilok, E. S. Takeuchi, D. Zhang, C. Jaye, *Science* **2019**, *366*, 645.
[29] Z. Y. Zheng, X. W. Zhong, Q. Zhang, M. T. Zhang, L. X. Dai, X. Xiao, J. H. Xu, M. L. Jiao, B. R. Wang, H. Li, Y. Y. Jia, R. Mao, G. M. Zhou, *Nat. Commun.* **2024**, *15*, 753.
[30] J. Xu, H. Li, Y. Jin, D. Zhou, B. Sun, M. Armand, G. Wang, *Adv. Mater.* **2024**, *36*, 2309726.
[31] Z. Yang, C. Lv, W. Li, T. Wu, Q. Zhang, Y. Tang, M. Shao, H. Wang, *Small* **2022**, *18*, 2104148.
[32] W. Yao, P. Zou, M. Wang, H. Zhan, F. Kang, C. Yang, *Electrochem. Energy Rev.* **2021**, *4*, 601.
[33] Zhang, L. Z., X. Jia, W. Song, Y. Liu, *Nano-Micro Lett.* **2024**, *16*, 75.
[34] Y. Tian, Y. L. An, Y. J. Yang, B. A. Xu, *Energy Storage Mater.* **2022**, *49*, 122.
[35] X. M. Xia, S. T. Xu, F. Tang, Y. Yao, L. F. Wang, L. Liu, S. N. He, Y. X. Yang, W. P. Sun, C. Xu, Y. Z. Feng, H. G. Pan, X. H. Rui, Y. Yu, *Adv. Mater.* **2023**, *35*, 2209511.
[36] S. W. Chee, S. F. Tan, Z. Baraissov, M. Bosman, U. Mirsaidov, *Nat. Commun.* **2017**, *8*, 1224.

© 2024 Wiley-VCH GmbH

15214095, 2024, 44, Downloaded from https://advanced.onlinelibrary.wiley.com/doi/10.1002/adma.202409763 by University Of Witwatersrand, Wiley Online Library on [12/12/2024]. See the Terms and Conditions (https://onlinelibrary.wiley.com/terms-and-conditions) on Wiley Online Library for rules of use; OA articles are governed by the applicable Creative Commons License

[37] Q. Liu, X. Liu, Y. Liu, M. Huang, W. H. Wang, Y. Cheng, H. Zhang, L. Xu, *ACS Nano* **2024**, *18*, 4932.
[38] H. Zhang, E. H. Kisi, *J. Alloys Compd.* **1997**, *248*, 201.
[39] M. Shimizu, K. Hirahara, S. Arai, *Phys. Chem. Chem. Phys.* **2019**, *21*, 7045.
[40] A. M. Rashidi, M. Hayati, A. Rezaei, *Solid State Sci.* **2011**, *13*, 1589.
[41] Y. Y. Li, H. L. Wong, J. Wang, W. L. Peng, Y. D. Shen, M. Y. Xu, Q. An, J. K. Kim, B. Yuan, W. A. Goddard, Z. T. Luo, *Adv. Energy Mater.* **2022**, *12*, 2202983.
[42] X. Zhou, R. P. Chen, E. H. Cui, Q. Liu, H. Zhang, J. H. Deng, N. N. Zhang, C. Xie, L. Xu, L. Q. Mai, *Energy Storage Mater.* **2023**, *55*, 538.
[43] M. Xi, Z. Liu, W. Wang, Z. Qi, R. Sheng, J. Ding, Y. Huang, Z. Guo, *Energy Environ. Sci.* **2024**, *17*, 3168.
[44] X. Z. Zhou, B. Wen, Y. C. Cai, X. M. Chen, L. Li, Q. Zhao, S. L. Chou, F. J. Li, *Angew. Chem., Int. Ed.* **2024**, *63*, 202402342.
[45] H. Z. Ren, S. Li, B. Wang, Y. Y. Zhang, T. Wang, Q. Lv, X. Y. Zhang, L. Wang, X. Han, F. Jin, C. Y. Bao, P. F. Yan, N. Zhang, D. L. Wang, T. Cheng, H. K. Liu, S. X. Dou, *Adv. Mater.* **2023**, *35*, 2208237.
[46] Z. Y. Liang, C. Li, D. X. Zuo, L. Zeng, T. Ling, J. J. Han, J. Y. Wan, *Energy Storage Mater.* **2023**, *63*, 102980.
[47] C. J. Vanoss, *Colloids Surf., A* **1993**, *78*, 1.
[48] C. Zhang, L. Gong, L. Xiang, Y. Du, W. Hu, H. Zeng, Z. K. Xu, *ACS Appl. Mater. Interfaces* **2017**, *9*, 30943.
[49] T. Chen, Y. A. Wang, Y. Yang, F. Huang, M. K. Zhu, B. T. W. Ang, J. M. Xue, *Adv. Funct. Mater.* **2021**, *31*, 2101607.
[50] D. Lv, H. L. Peng, C. Wang, H. X. Liu, D. D. Wang, J. Yang, Y. T. Qian, *J. Energy Chem.* **2023**, *84*, 81.
[51] D. Wang, H. Liu, D. Lv, C. Wang, J. Yang, Y. Qian, *Adv. Mater.* **2023**, *35*, 2207908.
[52] X. X. Song, L. Y. Bai, C. G. Wang, D. D. Wang, K. Xu, J. J. Dong, Y. L. Li, Q. Shen, J. Yang, *ACS Nano* **2023**, *17*, 15113.
[53] J. P. Chen, Y. Y. Shi, S. H. Zheng, W. Y. Zhao, R. M. Li, K. Ye, X. L. Zhao, Z. J. Zuo, Z. H. Pan, X. W. Yang, *Angew. Chem., Int. Ed.* **2024**, *63*, 2404825.
[54] Z. Y. Wu, C. J. Lu, Y. N. Wang, L. Zhang, L. Jiang, W. C. Tian, C. L. Cai, Q. F. Gu, Z. M. Sun, L. F. Hu, *Small* **2020**, *16*, 2000698.
[55] J. Wu, Q. Kuang, K. Zhang, J. J. Feng, C. M. Huang, J. J. Li, Q. H. Fan, Y. Z. Dong, Y. M. Zhao, *Energy Storage Mater.* **2021**, *41*, 297.
[56] C. Wang, D. D. Wang, D. Lv, H. L. Peng, X. X. Song, J. Yang, Y. T. Qian, *Adv. Energy Mater.* **2023**, *13*, 2204388.
[57] D. W. Sha, Y. R. You, R. X. Hu, X. Cao, Y. C. Wei, H. Zhang, L. Pan, Z. M. Sun, *Adv. Mater.* **2023**, *35*,2211311.
[58] S. H. Jiang, H. Wang, Y. Wu, X. J. Liu, H. H. Chen, M. J. Yao, B. Gault, D. Ponge, D. Raabe, A. Hirata, M. W. Chen, Y. D. Wang, Z. P. Lu, *Nature* **2017**, *544*, 460.
[59] Y. Z. Wang, X. M. Xu, J. Yin, G. Huang, T. C. Guo, Z. N. Tian, R. Alsaadi, Y. P. Zhu, H. N. Alshareef, *Adv. Mater.* **2023**, *35*, 2208171.
[60] Z. Y. Shen, J. L. Mao, G. P. Yu, W. D. Zhang, S. L. Mao, W. Zhong, H. Cheng, J. Z. Guo, J. H. Zhang, Y. Y. Lu, *Angew. Chem., Int. Ed.* **2023**, *62*, 2218452.
[61] C. P. Li, X. S. Xie, H. Liu, P. J. Wang, C. B. Deng, B. A. Lu, J. Zhou, S. Q. Liang, *Natl. Sci. Rev.* **2022**, *9*, nwab177.
[62] C. F. Liu, Y. Zhang, H. H. Cheng, X. X. Cai, D. Z. Jia, H. Lin, *Small* **2023**, *19*, 2301870.
[63] G. Kresse, J. Furthmüller, *Comput. Mater. Sci.* **1996**, *6*, 15.
[64] P. E. Blöchl, *Phys. Rev. B* **1994**, *50*, 17953.
[65] J. P. Perdew, K. Burke, M. Ernzerhof, *Phys. Rev. Lett.* **1996**, *77*, 3865.
[66] S. Grimme, J. Antony, S. Ehrlich, S. Krieg, *J. Chem. Phys.* **2010**,*132*, 154104.
[67] G. Henkelman, H. Jónsson, *J. Chem. Phys.* **2000**, *113*, 9978.

© 2024 Wiley-VCH GmbH

15214095, 2024, 44, Downloaded from https://advanced.onlinelibrary.wiley.com/doi/10.1002/adma.202409763 by University Of Witwatersrand, Wiley Online Library on [12/12/2024]. See the Terms and Conditions (https://onlinelibrary.wiley.com/terms-and-conditions) on Wiley Online Library for rules of use; OA articles are governed by the applicable Creative Commons License